OPEN ACCESS

Enhanced Carbon Dioxide Reduction Activity on Indium-Based Nanoparticles

Enhanced Carbon Dioxide Reduction Activity on Indium-Based Nanoparticles

James L. White* **and Andrew B. Bocarsly**,z**

Department of Chemistry, Princeton University, Princeton, New Jersey 08544, USA

Nanoparticles of indium, indium hydroxide, and indium oxide were synthesized and evaluated for their electrocatalytic abilities in the reduction of CO_2 to formate. These nanoparticles were characterized with several microscopic and spectroscopic techniques in order to investigate their structure and surface features. Their electrochemical behavior was also probed through voltammetry and bulk electrolysis. faradaic efficiencies approaching 100% were achieved on these particles at potentials as positive as −1.3 V vs. Ag/AgCl, which represents a significant decrease in the overpotential compared to that observed using bulk indium electrodes. The nanostructuring of the particles and the partial surface oxidation of the indium nanoparticles to yield catalytic surface indium hydroxide species are implicated in the high efficiencies at low overpotentials.
 [DOI: 10.1149/2.0681606jes]

Manuscript submitted January 22, 2016; revised manuscript received February 29, 2016. Published March 16, 2016.

Recent decades have seen the rapid rise in the amounts of carbon dioxide, a greenhouse gas, present in both the atmosphere and the oceans, as well as a concomitant increase in global temperatures.[1] This heating trend is predicted to amplify if net CO_2 emissions from fossil fuels continue to grow unabated, leading to a mean surface temperature increase of up to 4°C by 2100.[2] Therefore, a move away from fossil fuels toward renewable sources of energy such as wind and solar is essential for the long-term maintenance of the environment.

The reduction of carbon dioxide to fuels and chemicals is an important component of a future energy portfolio based on renewable sources that seeks to mitigate carbon levels. The formation of useful chemicals from CO_2 rather than petroleum decreases the net CO_2 emissions and reduces reliance on oil. Generating high energy density carbon-based fuels, though only carbon-neutral and not carbon-negative, aids in load-leveling with intermittent power sources, leading to the production of fuels during periods of high output and the consumption during periods of low output.

The electrochemical reduction of CO_2 on metal electrodes in aqueous solution has been studied for decades.[3] Heavy post-transition metals, including indium, tin, lead, and bismuth yield predominantly formate, with small amounts of CO and H_2 as well. These metals have high overpotentials for water reduction, which allows them to be more selective for CO_2 reduction than most transition metals. However, the CO_2 reduction overpotentials are also fairly large, typically on the order of 1 V, significantly decreasing the energy efficiency of conversion. These metals have been proposed to reduce CO_2 in a one-electron rate-determining step to the weakly adsorbed or free $CO_2^{\bullet-}$ radical anion, which can then be protonated and reduced by another electron to yield formate.[3] However, the formal redox potential for this process is −1.85 V vs. SHE,[4] considerably more negative than the potentials at which products are formed.

Recent, more in-depth investigations on the mechanism of formate production on these metals have led to a greater understanding of the role of surface species in the electrochemistry. Studies on tin[5,6] and indium[7,8] have demonstrated the importance of a hydrated oxide layer, either native or anodized, which can interact with CO_2 to form a surface-bound carbonate species that is implicated as an essential intermediate. Other research has shown that a size-dependence exists on gold,[9,10] palladium,[11] silver,[10,12,13] and tin oxide[14] nanoparticles for the conversion of CO_2, with an optimum diameter less than 10 nm but typically greater than 2 nm. Such nanoparticles have a high proportions of edge and corner sites, which, because of their lower coordination, are proposed to be more catalytically active than terrace atoms.[10]

We present here indium-based nanoparticles, which possess unusually high activity for CO_2 reduction to formate in aqueous solution at a range of potentials and pH values. The structural information obtained shows that the indium nanoparticles consist of a metallic core and a natively oxidized shell. These particles, in addition to the oxide and hydroxide nanoparticles, support the concept that an indium hydroxide surface is the active catalytic site for CO_2 reduction.

Experimental

Preparation of indium-based nanoparticles.—Indium nanoparticles (In NPs) were synthesized by the route published by Lim et al.[15] Briefly, 1 mL of oleylamine (70%, Sigma-Aldrich) was dissolved in 20 mL of *iso*-butylamine (Sigma-Aldrich) in a three-neck round-bottom flask equipped with a reflux condenser, which was evacuated to remove oxygen and then backfilled with nitrogen. 0.17 g $InCl_3$ (Sigma-Aldrich) was added to this solution and stirred for 15 minutes under N_2, after which 1 mL of 2 M $LiBH_4$ in THF was added dropwise. The resulting solution was stirred for an additional 15 minutes before heating to reflux at 70°C for 5 minutes. No visible reaction occurred until the silicone oil heating bath was at least 50°C, at which point the contents of the flask turned first pale yellow then eventually dark brown. The flask was allowed to cool and the nanoparticles were isolated by diluting the reaction mixture by a factor of 10 with 2-propanol (isopropanol, IPA, 99%, Sigma-Aldrich) and centrifuging at 13.3 krpm. The supernatant was discarded, and the process was repeated several times to remove unreacted $InCl_3$ and reaction byproducts.

Nanoparticles of indium oxide (In_2O_3) and indium hydroxide ($In(OH)_3$) were prepared as previously reported[7] and as originally described by Chandradass.[16] A ∼0.4 M solution of $In(NO_3)_3$ was precipitated with aqueous NH_4OH (28%, EMD) until a pH of 10 was reached, forming $In(OH)_3$. The $In(OH)_3$ particles were washed with ethanol, filtered, and dried overnight at 80°C. A portion of the $In(OH)_3$ was calcined at 400°C for 6 hours to yield In_2O_3.

Catalyst inks of the In, $In(OH)_3$, and In_2O_3 nanoparticles at ∼35 wt% on a metal basis were prepared by diluting the In reaction mixture with IPA or suspending the dried oxide or hydroxide particles in IPA by sonication, adding Vulcan XC-72 carbon black (Cabot), and sonicating for an hour to disperse the NPs onto the carbon. This suspension was centrifuged, the supernatant was removed, more IPA was added, and the contents were resuspended several times to clean the particles. Finally, 34 μL of 15% LIQUion solution (Ion Power, Inc.) per milliliter of suspension were added to serve as a binder

*Electrochemical Society Student Member.
**Electrochemical Society Member.
zE-mail: bocarsly@princeton.edu

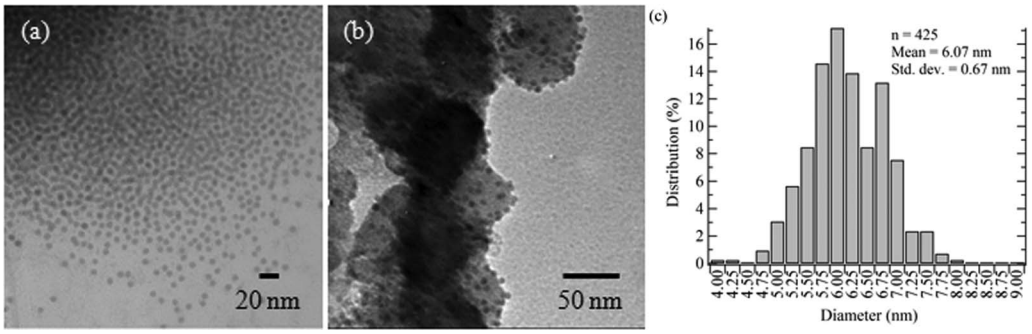

Figure 1. TEM micrographs of indium nanoparticles (a) as synthesized and (b) supported on carbon black. (c) Distribution of sizes of In NPs (n = 425).

for the ink. Tests showed that varying the amount of binder did not affect the electrochemical results significantly, except when minimal or low amounts of LIQUion were used and the catalyst flaked off the electrode.

Nanoparticle characterization.—Transmission electron microscopy (TEM) images of the nanoparticles were obtained using a Philips CM100 TEM at an accelerating voltage of 100 kV. Nanoparticle sizes were measured using an AMT Camera System. High-resolution TEM images were obtained with a Philips CM200 TEM at an accelerating voltage of 200 kV. X-ray diffraction (XRD) was performed on the NPs to determine their structure using a Bruker D8 Advance diffractometer with a 0.083° step size and Cu Kα radiation. A VG Scientific MK II ESCALab utilizing a magnesium X-ray source with a characteristic energy of 1253.6 eV and a hemispherical electron analyzer with a pass energy of 20 eV was employed to gather X-ray photoelectron spectroscopy (XPS) data. Samples of the In NPs were prepared via dropcasting the free nanoparticles from suspension onto carbon tape, whereas the In_2O_3 and $In(OH)_3$ samples were prepared by loading the dry powders on carbon tape and removing any excess before introducing to the vacuum chamber. Spectra were calibrated to the C 1*s* peak of adventitious carbon at a binding energy of 285 eV. Peak deconvolution with appropriate constraints was performed with the CasaXPS software package.

Electrochemical characterization of catalysts.—NP-based electrodes were prepared by dropcasting 10 μL of the respective catalyst inks 1 μL at a time onto a 3 mm diameter glassy carbon electrode (Bioanalytical Systems, Inc.) that had been polished with 1 μm alumina. Bulk indium metal disk electrodes were constructed using a piece of indium shot (99.999%, Sigma-Aldrich) set into a 2 mm diameter PTFE tube (McMaster-Carr) with a back electrical connection made via an embedded copper wire. For voltammetric experiments, the indium disk was polished to a mirror finish with 1 μm alumina, whereas, for bulk electrolyses, the surface was cleaved with a razor immediately prior to the commencement of the experiment to provide a fresh metallic surface.

Electrochemical experiments were conducted with an electrolyte of aqueous 0.5 M K_2SO_4 (99.0+%, Sigma-Aldrich) using CH Instruments 760 and 1140 potentiostats. Electrolyses performed at a pH of 7.5 utilized aqueous 0.5 M $KHCO_3$ (99.7+%, EMD). The reference electrodes were Ag/AgCl (3 M NaCl) (Bioanalytical Systems, Inc.), and all potentials presented here are referenced against this half-cell, unless otherwise noted. The counter electrodes were constructed of 1 cm^2 pieces of 100-mesh platinum gauze spot-welded to platinum wires (99.9%, Sigma-Aldrich). Cyclic voltammetry and bulk electrolyses were performed using three-neck round bottom flasks. For electrolyses, a counter electrode compartment composed of a fritted gas dispersion tube (Ace Glass) was used to separate the contents of the flask, including any products that may have formed, from the oxidative processes at the platinum mesh counter electrode. All solutions were pre-purged with argon or carbon dioxide (AirGas) for 20 minutes prior to the commencement of electrochemical experiments; during electrolyses the solution continued to be purged, whereas for cyclic voltammetry only the headspace was maintained with a gentle but constant flow of the appropriate gas. Current densities are reported with respect to the geometric surface area of the glassy carbon disk and do not factor in the roughness of the nanoparticle-laden carbon black.

Product detection and analysis.—Liquid-phase products were analyzed by nuclear magnetic resonance (NMR) spectroscopy using a Bruker Avance III 500 MHz system with a cryoprobe detector. A special water excitation sculpting solvent suppression pulse sequence tuned for use with salty solutions was employed for enhanced sensitivity. A 1,4-dioxane (Sigma-Aldrich) internal standard was included with each sample. Faradaic efficiencies were determined based on the quantities of detected products and the total amount of charge passed.

Results and Discussion

Characterization of indium nanoparticles.—The synthesized indium nanoparticles as imaged by TEM (Figure 1) were found to be highly monodisperse, with an average diameter of 6.1 ± 0.7 nm. When incorporated onto carbon black (CB), the In NPs were distributed fairly evenly with no observed agglomeration or change in size.

The $In(OH)_3$ and In_2O_3 particles were slightly larger and more irregularly shaped than the In NPs, as shown in Figure 2. The $In(OH)_3$ NPs were 8.11 ± 1.87 nm in diameter, whereas the In_2O_3 NPs were 9.77 ± 3.29 nm, likely because of some agglomeration during the annealing process. The constituents of these two sets of particles clustered together considerably more than the In NPs, since the presence of surfactant on the In NPs likely prevented significant inter-particle adhesion.

X-ray diffraction patterns for each set of particles are depicted in Figure 3, along with literature patterns for In, $In(OH)_3$, and In_2O_3. While the $In(OH)_3$ NPs were predominantly amorphous, the other

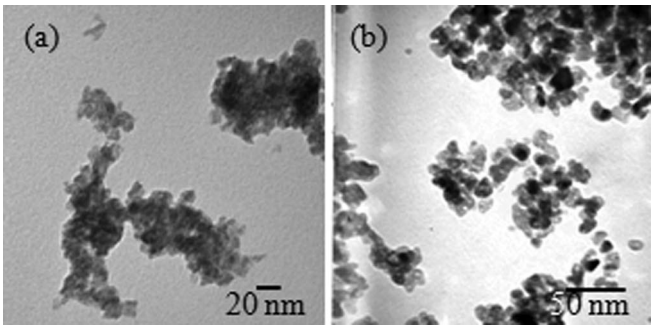

Figure 2. TEM micrographs of (a) $In(OH)_3$ nanoparticles prepared by precipitation and (b) In_2O_3 nanoparticles formed by annealing the $In(OH)_3$ particles at 400°C.

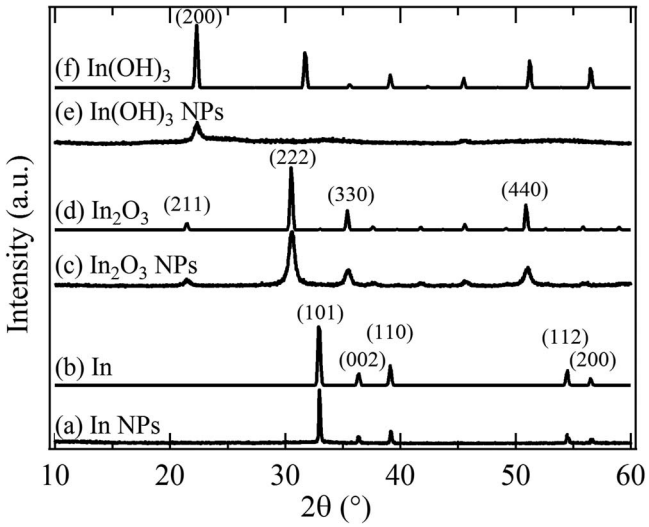

Figure 3. X-ray diffraction patterns of (a) In NPs, (c) In_2O_3 NPs, and (e) $In(OH)_3$ NPs, with corresponding literature patterns of (b) In,[29] (d) In_2O_3,[30] and (f) $In(OH)_3$.[29] The assigned lattice planes of the major peaks are indicated.

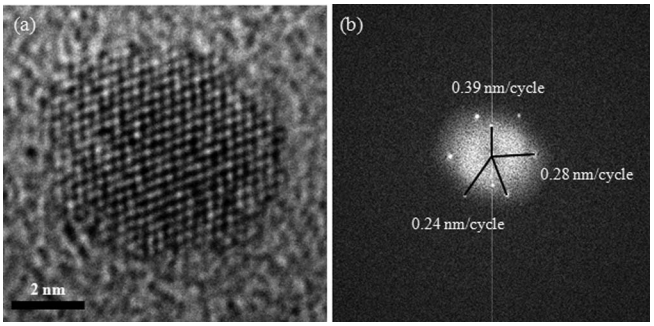

Figure 5. (a) HRTEM image of an indium nanoparticle. (b) Fast Fourier transform of the micrograph showing the diffraction points from the crystal planes.

two sets had high degrees of crystallinity and matched the respective literature patterns well, with no detected impurity phases. By refinement of the diffraction patterns, the lattice parameters were found to be $a = 0.325$ nm and $c = 0.496$ nm for the tetragonal I4/mmm In NPs, whereas the lattice parameter for the cubic $Ia\bar{3}In_2O_3$ NPs was $a = 1.013$ nm.

Calibrated O 1*s* (left) and In 3*d* (right) regions of the XPS spectra of each type of nanoparticle are shown in Figure 4, with the raw data presented as the solid black lines. Due to the small size of the nanoparticles, it is expected that the characteristic photoelectrons would be able to penetrate through the particles and thus, sample the entire volume of each particle. The In NP sample (Figure 4a), unlike the oxide samples, showed a high binding-energy peak ~534 eV (wide gray dashes) which is attributable to residual 2-propanol from the cleaning process. The peak at ~532 eV (black hashes) in the In NP and In_2O_3 NP spectra is assigned to an indium hydroxide since it is the only feature observed in the $In(OH)_3$ NP spectrum (Figure 4c). The feature at ~529 eV (black dashes) in the In NP and In_2O_3 NP corresponds to indium oxide. These assignments are consistent with those previously described in the literature.[7,17,18] Though the In_2O_3 NPs still retain significant oxide character, they gained hydroxide moieties, likely through hydration from ambient water vapor. Peaks corresponding to oxygen vacancies, as seen in other, similar systems,[19,20] were not observed in any of these spectra.

In the indium spectra, peaks near 452 and 444.5 eV (black hashes and dashes, respectively) correspond to the In $3d_{3/2}$ and In $3d_{5/2}$ signals, respectively, for an In^{3+} species, whereas the peaks at 451 and 444 eV (gray hashes and dashes, respectively), correspond to the presence of an In^0 species, in accordance with previous literature.[21] The small, solid gray peaks are In $3d_{3/2}$ satellites, which are shifted 8.4 eV relative to the main peaks, resulting from the nonmonochromaticity of the magnesium X-ray source. Similar In $3d_{5/2}$ satellites, which were not fit, are visible at the low binding energy end of the detailed spectral region. For both $In(OH)_3$ and In_2O_3, only peaks for oxidized indium are apparent, at 452.0 eV and 451.6 eV for the In $3d_{3/2}$ signal and 444.5 eV and 444.1 eV for the In $3d_{5/2}$ signal, respectively. In contrast, two pairs of peaks appear in the deconvolution of the indium region of the In NPs, indicating that both an In^{3+} species (452.4 and 444.7 eV) and an In^0 species (451.3 and 443.8 eV) are present in the sample. The predominance of the metallic peaks shows that the majority of the sample remains unoxidized, as the XRD pattern would suggest. Taken together the XRD and XPS data suggest that the oxidized In^{3+} species is present as a thin shell on the surface of a pure In metallic core.

To confirm this possibility of a core-shell structure, the indium nanoparticles were examined by HRTEM (Figure 5). Several lattice fringe spacings were evident on the particles as determined from both the images and fast Fourier transforms thereof: 0.28 nm, 0.24 nm, and 0.39 nm. The lattice spacing of 0.28 nm, which was most predominant, coincides with the *d* value expected for the In (101) plane (0.272 nm), as well as that for the $In(OH)_3$ (220) plane (0.281 nm), using the lattice parameters obtained from the XRD patterns above. The value of

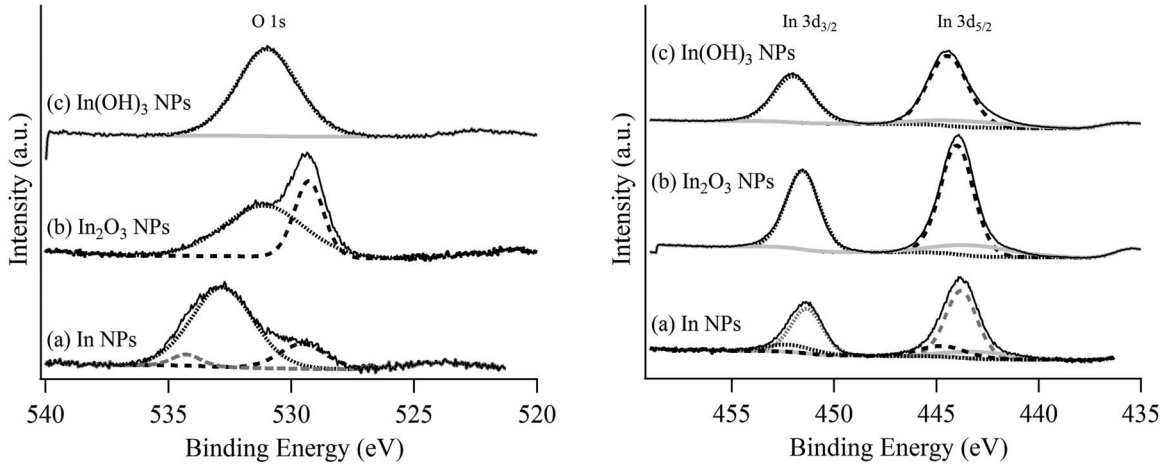

Figure 4. XPS spectra showing the O 1*s* (left) and In 3*d* (right) regions of (a) In NPs, (b) In_2O_3 NPs, and (c) $In(OH)_3$ NPs. Spectra have been calibrated against the adventitious carbon 1*s* signal. An adjustment of 8 eV was required to calibrate spectrum (c) because of charging due to the nonconducting nature of $In(OH)_3$.

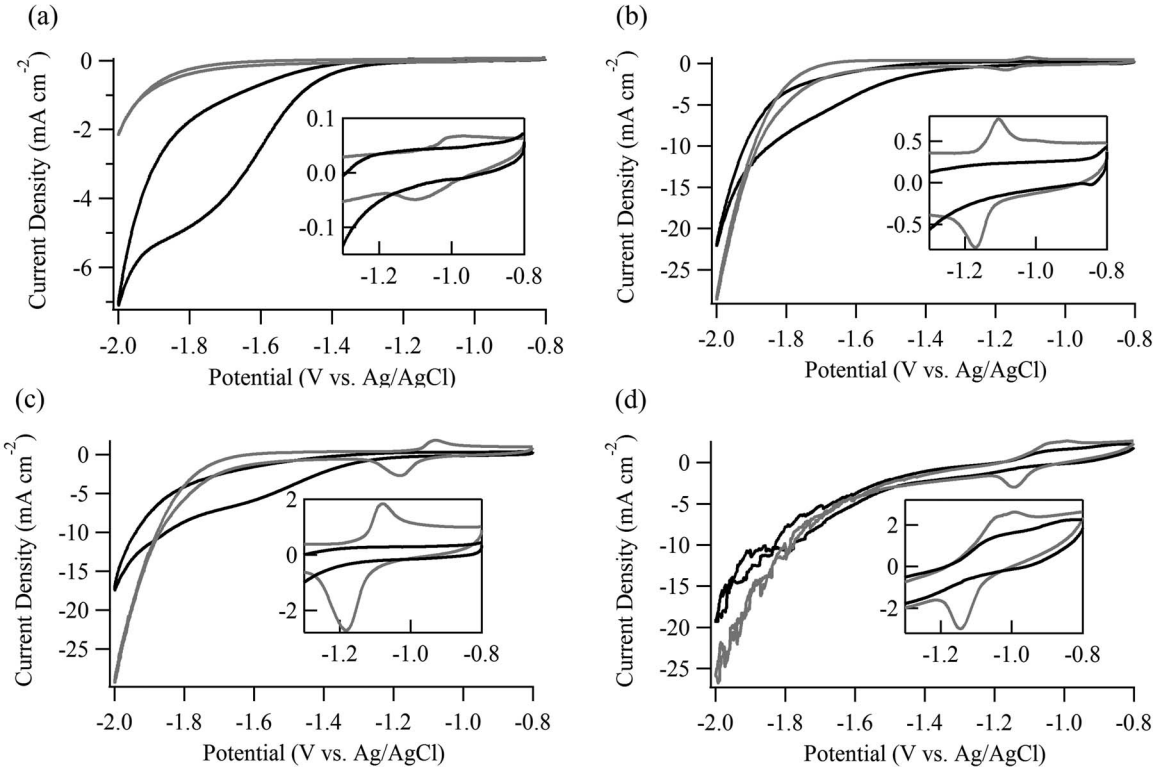

Figure 6. Cyclic voltammograms at 25 mV/s of (a) In NPs, (b) $In(OH)_3$ NPs, (c) In_2O_3 NPs, and (d) bulk In disk in Ar- (gray) and CO_2-saturated (black) 0.5 M K_2SO_4. Insets show the region between −1.3 V and −0.8 V for each catalyst.

0.24 nm is closest to the In_2O_3 (330) plane spacing (0.239 nm), and 0.39 nm is most closely matched with the $In(OH)_3$ (200) plane. All three observed lattice spacings cannot be explained by a single species, indicating that the nanoparticles were mixtures of indium metal, oxide, and hydroxide. This conflicts with previously reported HRTEM imaging of indium nanoparticles prepared by an evaporation method, which were found to have the same spacing of 0.277 nm but which was attributed to the (111) plane of cubic indium with a lattice parameter of 0.50 nm.[22] A distinct core-shell structure could not be observed in the present study, though the spherical aberration from the electron beam may have contributed to the extension of lattice fringes beyond their true location.[23]

Electrochemical studies.—Cyclic voltammograms in both Ar- and CO_2-saturated 0.5 M $K_2SO_{4(aq)}$ of the three nanoparticle catalysts supported on glassy carbon, as well as of a polished bulk indium disk electrode, are presented in Figure 6. In all cases the electrolyte pH was adjusted to 5.3. Current enhancement under CO_2 is evident in all of the comparisons, though most particularly with the In NPs and least so with the In disk. At highly negative potentials, all of the electrodes begin to reduce water, but the bulk In disk produces significant enough quantities of H_2 that the current trace is disturbed by bubble formation, in contrast to the supported nanoparticle electrodes.

The insets in Figure 6 depict the potential regions between −1.3 V and −0.8 V for each of the catalyst materials. The set of waves shown

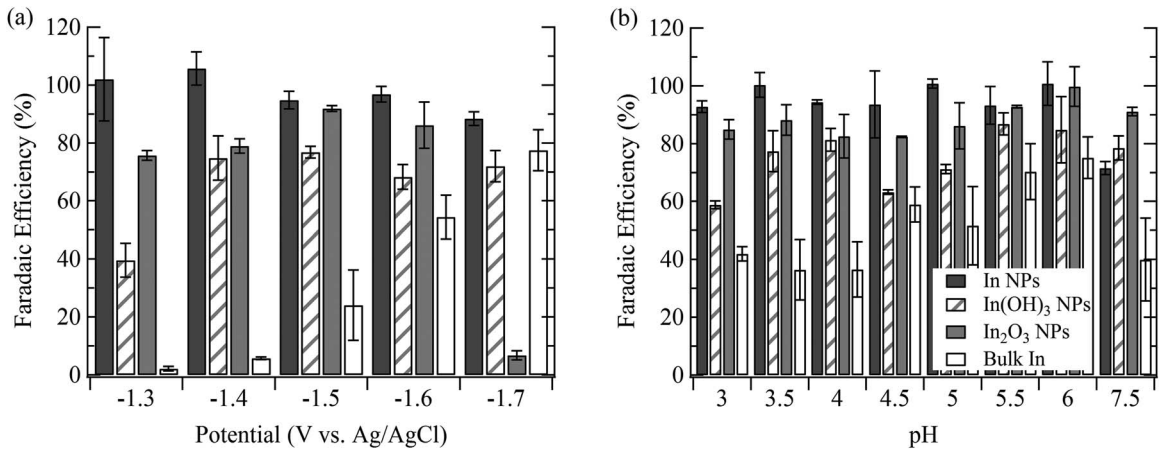

Figure 7. Average faradaic efficiencies of formate for bulk electrolyses conducted at (a) various potentials and (b) a range of pH values on the In NPs (dark gray) $In(OH)_3$ NPs (diagonal hatching), In_2O_3 NPs (light gray), and a metallic bulk In disk (white). Error bars indicate standard deviations of multiple experiments at identical conditions.

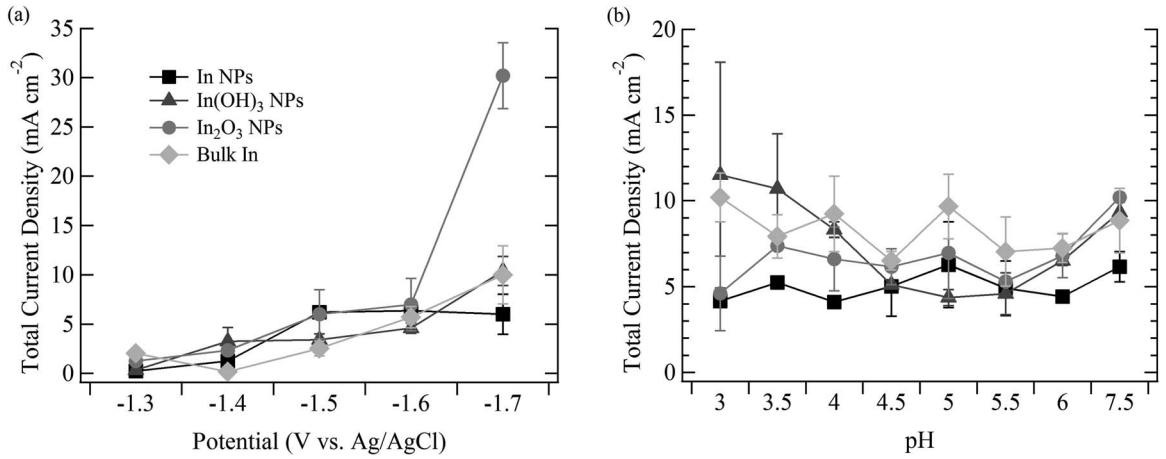

Figure 8. Average current densities of the electrolyses performed at a range of (a) potentials and (b) pH values with the In-based catalysts In NPs (squares), $In(OH)_3$ NPs (triangles), In_2O_3 NPs (circles), and bulk In disk (diamonds). Error bars indicate standard deviations of multiple experiments at identical conditions.

corresponds to the reduction and reoxidation of either indium hydroxide and indium oxide, both of which have formal reduction potentials around −1.2 V vs. Ag/AgCl.[24] The magnitude of this couple is significantly greater relative to the background capacitance with the In_2O_3 particles than with any of the other species, indicating that the $In(OH)_3$ is somewhat less readily reduced than the oxide. In addition, this reduction event appears under argon, but is absent under carbon dioxide on the nanoparticles. Previous work has established the existence of a surface indium carbonate (In-CO_3^-) at reducing potentials in the presences of CO_2.[7] This carbonate species is electrosilent in the inset potential window, though turnover of this species can occur, as indicated by the onset of CO_2 current enhancement, at slightly more negative potentials. The absence of a reoxidation wave under CO_2 indicates that, though the In-CO_3^- is reduced, In^0, which would be reoxidizable to In^{3+}, is not formed. Instead, the current passes to the bound CO_2.

Bulk electrolyses were conducted in triplicate at a range of both potentials and pH values in 0.5 M $K_2SO_{4(aq)}$ under continuous CO_2 bubbling in order to interrogate the efficiencies of the nanoparticle catalysts and compare them to those of bulk indium. The pH 7.5 electrolyses were performed in 0.5 M $KHCO_{3(aq)}$. The potential and pH dependence of the faradaic efficiencies, ξ_F, for formate are shown in Figure 7. Each of the electrolyses in the potential study was conducted at a pH of 5.3, and the pH study electrolyses were each performed at a potential of −1.6 V. The total current density over the course of each experiment was fairly consistent, though there was some variability between experiments at the same conditions due to slight variations in electrode preparation and CO_2 purging (Figure 8). During each experiment employing 0.5 M K_2SO_4, which, unlike $KHCO_3$, does not contain an explicit buffer system, the local pH near the electrodes may have varied significantly from that of the bulk solution.

The faradaic efficiency for the In NPs was uniformly high, nearly 100%, across a wide range of both potentials and pHs. Slight decreases in relative formate production were apparent at the most acidic pH and at the most negative potential because of increases in the rate of hydrogen evolution under these conditions. In comparison, the metallic indium disk had low ξ_F values at low overpotentials, not even exceeding 50% until −1.6 V. The In disk efficiencies were also consistently less than the In NPs across the pH range studied.

The $In(OH)_3$ and In_2O_3 NPs had somewhat lower efficiencies than the In NPs, but were still fairly consistent at various pHs and potentials. At −1.3 V, the $In(OH)_3$ NPs had relatively low ξ_F, likely resulting from their fairly insulating nature and the need for additional potential to effect reduction of CO_2 through the amorphous nanoparticles. The In_2O_3 NPs, which were considerably more conductive and crystalline, had high efficiencies between −1.3 and −1.6 V; however, at −1.7 V, formation of bubbles, likely hydrogen, predominated, allowing little charge to pass to CO_2. This change may also have resulted from the reduction of the oxide nanoparticles to more metallic species, which would also consume some electrons and reduce the effectiveness of the catalysts. Although the Pourbaix diagram for indium would suggest otherwise,[25] both $In(OH)_3$ and In_2O_3 were sufficiently stable in fairly acidic solutions at negative potentials to generate formate with high yields.

The variations in pH resulted in very little change in faradaic efficiencies for any of the catalysts. Since CO_2 was constantly replenished, its concentration remained constant at its saturation level of 33 mM. However, as the pH increases, greater concentrations of dissolved bicarbonate are present (15 μM at a pH of 3 vs. 15 mM at a pH of 6 in K_2SO_4). Even in the 0.5 M $KHCO_3$ solution at pH = 7.5, ξ_F values were not significantly different than at more acidic conditions. This trend indicates that dissolved CO_2, not HCO_3^-, is the electrochemical substrate, since no ξ_F dependence on HCO_3^- concentration is evident and current densities remained fairly consistent across the pH range. This finding echoes that of previous work, which showed that utilizing pressurized CO_2 to increase aqueous CO_2 concentrations led to higher reduction peak current densities on indium.[7]

Modifications of the In NPs were conducted in order to ascertain the cause of the enhanced activity. For example, the 18-carbon oleylamine surfactant may have enhanced the local CO_2 concentration relative to that of water near the nanoparticle surfaces due to its nonpolar character. Acetic acid (HOAc) was employed in attempts to remove this surfactant from the particles, as had been done with Pt nanoparticles.[26] The In NPs were sonicated in 10% HOAc in IPA, for 60 min before being centrifuged and resuspended in the same solvent mixture. These 10% HOAc-suspended particles were slightly larger (13.2 ± 7.1 nm diameters) than the untreated set, due to acid-catalyzed Ostwald ripening, leading to the growth of larger particles at the expense of the smallest particles. However, when these nanoparticles were suspended on carbon and electrolyses were performed with them, the faradaic efficiencies were similar to those of the untreated In NPs (Figure 9).

Because the dilute acetic acid treatment may have been insufficient to remove the oleylamine completely, other batches of nanoparticles were prepared without any of the oleylamine surfactant. The nanoparticle sizes did not differ substantially from those of the NPs synthesized with oleylamine, indicating that the isobutylamine solvent used in the synthesis, rather than just the oleylamine, acted as a capping agent for nanoparticle growth, though there was also some more amorphous material visible by TEM. The electrolysis currents and faradaic efficiencies of these particles were again similar to those of the originally synthesized In NPs (Figure 9). The absence of the long surfactant had no significant effect on the electrochemical behavior of the indium nanoparticles, revealing that the nonpolar chain does not

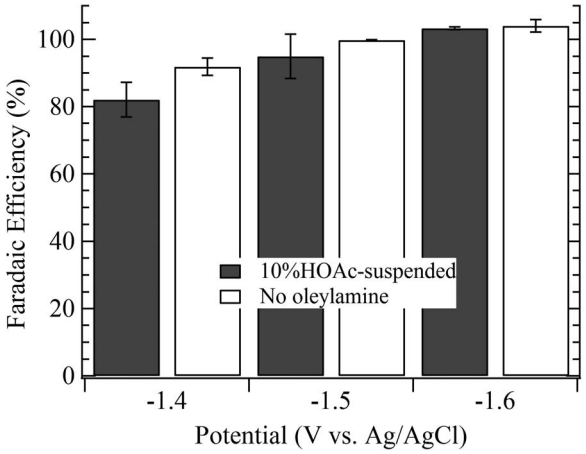

Figure 9. Faradaic efficiencies of CO_2 reduction to formate in pH 5.3 0.5 M K_2SO_4 with In NPs (gray) suspended in 10% HOAc and (white) synthesized without oleylamine. Error bars indicate standard deviations of multiple experiments at identical conditions.

substantially promote the concentration of CO_2 near the nanoparticle surface.

Based on these data, the enhanced activity of the In NPs for carbon dioxide reduction, particularly at low overpotentials, is due to several factors. The nanoparticles, which were synthesized in the metallic form, oxidize rapidly but incompletely in air and aqueous solution, yielding particles that have both In^0 and In^{3+} species, with the latter most likely on the exterior. Complete oxidation does not occur due to the passivation of the surface by the oxide shell, as in other metal nanoparticle systems.[27] Based on the oxygen XPS data, the In^{3+} species is predominantly an indium hydroxide, which has previously been implicated as the catalytic resting state for CO_2 reduction on indium and the site at which CO_2 can chemisorb and be reduced as the carbonate.[7] The metallic core provides a conductive path for electrons to flow from the carbon black support to the catalytic surface, unlike in the pure In_2O_3 and $In(OH)_3$ particles, which are more insulating and allow the carbon black to evolve hydrogen. The In NPs significantly outperform the bulk indium, even though both have some surface oxyhydroxide moieties, because the nanoparticles, with their small size, have a much greater radius of curvature and thus would possess a larger proportion of high-energy edge and corner sites. The activity of these sites is likely considerably higher because more of the indium atoms will be oxidized in an effort to fill their partially vacant coordination spheres, and the pendant oxygen species on these indium atoms will also have low coordination numbers and thus greater ability to bind CO_2 and reduce it. Bulk indium, especially when freshly polished or cleaved, would have fewer surface oxygens and thus not be able to reduce CO_2 as effectively at low overpotentials. In addition, recent work on thin films of gold inverse opal suggests that differential mass transport in mesoporous materials, such as the carbon black support used in this study, may alter the selectivity of CO_2 reduction compared to H_2 production, leading to a suppression of proton and solvent reduction.[28]

Conclusions

The electrochemical reduction of CO_2 on metal nanoparticles has been reported previously, primarily in the context of the nanoparticle sizes. In this study, the importance of the natively formed indium oxide and hydroxide on the surface of metallic indium NPs has been demonstrated, leading to unit faradaic efficiencies for formate across a wide range of potentials and pH conditions. Nanoscale In_2O_3 and $In(OH)_3$ also had high efficiencies, considerably greater than those reported on bulk indium, both native and anodized. It is suggested that the high activities of the nanoparticles, which were less than 10 nm in diameter, were due in part to the nanostructuring of the material, which exposes more high-energy edges than in the bulk, and to the presence of oxidized indium moieties, which have previously been implicated as the catalytic species for CO_2 reduction through the formation of surface carbonates.

Acknowledgments

The authors acknowledge the National Science Foundation (grant CHE-1308652) for financial support for this work. James Pander III and Maor Baruch are thanked for fruitful discussions. We thank John Schreiber for invaluable assistance with microscopy and Kenith Conover for help with NMR. Matthew Vallon, Jessica Frick, and Prof. Robert Cava assisted with X-ray photoelectron spectroscopy and X-ray diffractometry, respectively. The manuscript was written through contributions of both authors. Both authors have given approval to the final version of the manuscript. ABB is a co-founder and president of the Scientific Advisory Board holding less than a 5% interest in Liquid Light, Inc., a company focused on the electrochemical conversion of carbon dioxide to chemicals.

References

1. D. L. Hartmann, A. M. G. Klein Tank, M. Rusticucci, L. Alexander, S. Broennimann, Y. Abdul-Rahman Charabi, F. Dentener, P. Thorne, M. Wild, and P. Zhai, in *Climate Change 2013: The Physical Science Basis. Contribution of Working Group I to the IPCC Fifth Assessment Report*, T. F. Stocker, D. Qin, G.-K. Plattner, M. Tignor, S. K. Allen, J. Boschung, A. Nauels, Y. Xia, V. Bex, and P. M. Midgley, Editors, Cambridge University Press, New York (2014) http://ipcc.ch/pdf/assessment-report/ar5/wg1/WG1AR5_Chapter02_FINAL.pdf.
2. M. Collins, Reto Knutti, Julie Arblaster, Jean-Louis Dufresne, Thierry Fichefet, Piere Friedlingstein, Xuejie Gao, William J. Gutowski Jr., Tim Johns, Gerhard Krinner, Mxolisi Shongwe, Claudia Tebaldi, Andrew J. Weaver, and Michael Wehner, in *Climate Change 2013: The Physical Science Basis. Contribution of Working Group I to the IPCC Fifth Assessment Report*, Sylvie Joussaume, Abdalah Mokssit, Karl Taylor, and Simon Tett, Editors, Cambridge University Press, New York (2014) http://www.climatechange2013.org/images/report/WG1AR5_Chapter12_FINAL.pdf.
3. Y. Hori, H. Wakebe, T. Tsukamoto, and O. Koga, *Electrochimica Acta*, **39**, 1833 (1994).
4. P. S. Surdhar, S. P. Mezyk, and D. A. Armstrong, *J. Phys. Chem.*, **93**, 3360 (1989).
5. Y. Chen and M. W. Kanan, *J. Am. Chem. Soc.*, **134**, 1986 (2012).
6. M. F. Baruch, J. E. Pander, J. L. White, and A. B. Bocarsly, *ACS Catal.*, **5**, 3148 (2015).
7. Z. M. Detweiler, J. L. White, S. L. Bernasek, and A. B. Bocarsly, *Langmuir*, **30**, 7593 (2014).
8. K. K. Ghuman, T. E. Wood, L. B. Hoch, C. A. Mims, G. A. Ozin, and C. V. Singh, *Phys. Chem. Chem. Phys.*, **17**, 14623 (2015).
9. W. Zhu, R. Michalsky, O. Metin, H. Lv, S. Guo, C. J. Wright, X. Sun, A. A. Peterson, and S. Sun, *J. Am. Chem. Soc.*, **135**, 16833 (2013).
10. S. Back, M. S. Yeom, and Y. Jung, *ACS Catal.*, **5**, 5089 (2015).
11. D. Gao, H. Zhou, J. Wang, S. Miao, F. Yang, G. Wang, J. Wang, and X. Bao, *J. Am. Chem. Soc.*, **137**, 4288 (2015).
12. A. Salehi-Khojin, H.-R. M. Jhong, B. A. Rosen, W. Zhu, S. Ma, P. J. A. Kenis, and R. I. Masel, *J. Phys. Chem. C*, **117**, 1627 (2013).
13. J. Rosen, G. S. Hutchings, Q. Lu, S. Rivera, Y. Zhou, D. G. Vlachos, and F. Jiao, *ACS Catal.*, **5**, 4293 (2015).
14. S. Zhang, P. Kang, and T. J. Meyer, *J. Am. Chem. Soc.*, **136**, 1734 (2014).
15. T. H. Lim, B. Ingham, K. H. Kamarudin, P. G. Etchegoin, and R. D. Tilley, *Cryst. Growth Des.*, **10**, 3854 (2010).
16. J. Chandradass, D. S. Bae, and K. H. Kim, *Adv. Powder Technol.*, **22**, 370 (2011).
17. Z. M. Detweiler, S. M. Wulfsberg, M. G. Frith, A. B. Bocarsly, and S. L. Bernasek, *Surf. Sci.* (2015).
18. J.-C. Dupin, D. Gonbeau, P. Vinatier, and A. Levasseur, *Phys. Chem. Chem. Phys.*, **2**, 1319 (2000).
19. J. C. C. Fan and J. B. Goodenough, *J. Appl. Phys.*, **48**, 3524 (1977).
20. L. B. Hoch, T. E. Wood, P. G. O'Brien, K. Liao, L. M. Reyes, C. A. Mims, and G. A. Ozin, *Adv. Sci.*, **1**, 1400013 (2014).
21. R. W. Hewitt and N. Winograd, *J. Appl. Phys.*, **51**, 2620 (1980).
22. B. Balamurugan, F. E. Kruis, S. M. Shivaprasad, O. Dmitrieva, and H. Zähres, *Appl. Phys. Lett.*, **86**, 083102 (2005).
23. N. Tanaka, *Sci. Technol. Adv. Mater.*, **9**, 014111 (2008).
24. P. Vanýsek, in *CRC Handbook of Chemistry and Physics*, W. M. Haynes, T. J. Bruno, and D. R. Lide, Editors, p. 80, CRC Press, New York (2012).
25. M. Pourbaix, in *Atlas of Electrochemical Equilibria in Aqueous Solutions*, p. 72,436, National Association of Corrosion Engineers, Houston, TX (1974).
26. D. Li, C. Wang, D. Tripkovic, S. Sun, N. M. Markovic, and V. R. Stamenkovic, *ACS Catal.*, **2**, 1358 (2012).

27. H. Bi, W. Cai, C. Kan, L. Zhang, D. Martin, and F. Träger, *J. Appl. Phys.*, **92**, 7491 (2002).
28. A. S. Hall, Y. Yoon, A. Wuttig, and Y. Surendranath, *J. Am. Chem. Soc.*, **137**, 14834 (2015).
29. D. F. Mullica, G. W. Beall, W. O. Milligan, J. D. Korp, and I. Bernal, *J. Inorg. Nucl. Chem.*, **41**, 277 (1979).
30. F. L. Faita, C. E. M. Campos, K. Ersching, and P. S. Pizani, *Mater. Chem. Phys.*, **125**, 257 (2011).